Earth Surf. Dynam. Discuss., 3, 83–128, 2015
www.earth-surf-dynam-discuss.net/3/83/2015/
doi:10.5194/esurfd-3-83-2015

Earth Surface Dynamics
Discussions
Open Access

Millennial erosion rates across the Pamir based on ^{10}Be concentrations in fluvial sediments: dominance of topographic over climatic factors

M. C. Fuchs[1,2], R. Gloaguen[1,3], S. Merchel[4], E. Pohl[1], V. A. Sulaymonova[1], C. Andermann[5], and G. Rugel[4]

[1]Remote Sensing Group, Institute of Geology, TU Bergakademie Freiberg, Bernhard-von-Cotta-Strasse 2, 09599 Freiberg, Germany
[2]Section Periglacial Research, Alfred-Wegener-Institute for Polar and Marine Research, Telegraphenberg A43, 14473 Potsdam, Germany
[3]Remote Sensing Group, Helmholtz-Zentrum Dresden-Rossendorf, Helmholtz Institute Freiberg for Resource Technology, Halsbrücker Strasse 34, 09599 Freiberg, Germany
[4]Helmholtz-Zentrum Dresden-Rossendorf, Helmholtz Institute Freiberg for Resource Technology, Bautzner Landstrasse 400, 01328 Dresden, Germany
[5]Section 5.1 Geomorphology, German Research Centre for Geoscience GFZ, Telegraphenberg, 14473 Potsdam, Germany

Received: 17 November 2014 – Accepted: 9 December 2014 – Published: 29 January 2015

Correspondence to: M. C. Fuchs (fuchsm@mailserver.tu-freiberg.de)

Published by Copernicus Publications on behalf of the European Geosciences Union.

Abstract

The understanding of erosion processes is fundamental to study the evolution of actively deforming mountain ranges, whereas the relative contributions tectonic and climatic factors and their feedbacks are debated. The Pamir is peculiar in both, high deformation rates induced by the India–Eurasia collision and its position at the transition between Westerlies and Monsoon. In order to contribute to this debate we quantify basin-wide erosion rates from cosmogenic ^{10}Be concentrations in modern river sediments measured by accelerator mass spectrometry. Sample locations represent the Panj basin at six sites along its trunk stream, and the major, east–west elongated tributary basins at five sites. An average erosion of $\sim 0.64\,\mathrm{mm\,yr^{-1}}$ for the entire Pamir reveals a rapid landscape evolution. Erosion rates of tributary sub-basins highlight the strong contrast between the plateau (0.05 to $0.16\,\mathrm{mm\,yr^{-1}}$) and the Pamir margins (0.54 to $1.45\,\mathrm{mm\,yr^{-1}}$).

The intensity of erosion is primarily (R^2 of 0.81) correlated to slope steepness (0.75 quartiles) suggesting either tectonic uplift or base level lowering. Multiple linear regression reveals that precipitation may contribute also to the efficiency of erosion (R^2 of 0.93) to a lesser extent. Dry conditions and low slopes hinders sediment transport and consequently, erosion on the plateau. The highest erosion coincides with the predominant winter precipitation from the Westerlies. The concentrated discharge during spring and early summer favors pronounced erosion along the north-western Pamir margin by driving the sediment flux out of the basins. The magnitude of erosion in Pamir is similar to rates determined in the south Himalayan escarpment, whereas climatic and tectonic conditions are very different. Millennial erosion does not balance the roughly ten times higher fluvial incision implying a transient landscape. We propose that river captures are responsible for the strong base level drop driving the incision along the Panj and consequently, initiate steep hillslopes that will contribute to high erosion at the Pamir margins. Precipitation may act as limiting factor to hillslope adjustment and consequently to erosion processes.

1 Introduction

Several recent studies with a focus on high mountains highlight the complexity of the interactions between tectonically triggered rock uplift and climate-driven processes, and their respective roles on erosion rates (e.g. Montgomery and Brandon, 2002; Burbank et al., 2003; Huntington et al., 2006; Godard et al., 2012, 2014). Spatial and temporal variations of erosion rates allow to constrain the specific factors that control mountain evolution (e.g. Molnar and England, 1990; Burbank and Anderson, 2000). But erosion in turn also affects tectonic processes for example by inducing a sediment flux out of the orogen and a mass loss that will be compensated by isostatic uplift (e.g. Molnar and England, 1990; Champagnac et al., 2009).

The peculiar tectonic and climatic setting of the Pamir provides the necessary conditions that allow to study erosion in response to variable drivers. The orogen lies at the westernmost part of the India–Asia collision zone, one of the Earth's largest and most rapidly deforming intra-continental convergence zone (e.g. Reigber et al., 2001; Mohadjer et al., 2010). This position coincides with the transition between the atmospheric circulation systems of the Indian Summer Monsoon (ISM) and the Westerlies, making this region particularly interesting when studying the role of climate in evolving mountains. However, the magnitude of erosion and the factors behind spatial and temporal variations are poorly constrained in the Pamir. So far, erosion was only studied in the context of the mainly Miocene dome exhumation in the southern Pamir. Stübner et al. (2013) inferred roughly 0.5 $mm\,yr^{-1}$ from thermochronological modelling of the peak exhumation and geometric reconstructions of the Shakhdara Dome. Such long-term erosion integrates over variable climatic conditions during the Quaternary and cannot resolve spatial variations of the erosional response to climatic gradients or changes in uplift across the Pamir.

Regional studies of erosion rates in the India–Asia collision zone concerned mainly the southern escarpment of the Himalayas. Variations in erosion were found to correlate to long-term climate fluctuations that govern glacial processes (Gabet et al., 2008;

Discussion Paper | Discussion Paper | Discussion Paper | Discussion Paper |
ESURFD
3, 83–128, 2015

Godard et al., 2012) and the intensity of the ISM (e.g. Bookhagen et al., 2005). Links between precipitation and erosion correspond also to regional relief characteristics that induce orographic effects (e.g. Garzanti et al., 2007; Gabet et al., 2008). Orographic rain shadow leads to a shift from precipitation- to temperature-sensitive erosion across the southern Himalayan escarpment resulting in an increased influence of concentrated peak discharge during the melting season on erosion (e.g. Burbank et al., 2012). Additionally, the availability of sediment to be transported (Burbank et al., 2012) and the magnitude-frequency distribution of direct runoff (Andermann et al., 2012) modulate rates of erosion. The generation of sediment and direct runoff are genetically linked to slope or relief as a consequence of base level lowering, hillslope thresholds or landslide frequency, factors that were found to control erosion (e.g. Montgomery and Brandon, 2002; Ouimet et al., 2009). In particular, the correlation between erosion and long-term tectonic uplift in the Greater Himalaya is debated as rates are suggested to adjust fast to climatic variations (Burbank et al., 2003; Godard et al., 2014).

The debated control factors outline the fact that measured erosion rates highly depend on the chosen method and the captured time interval (e.g. Garzanti et al., 2007; Lupker et al., 2012). The short-term variability in erosion rates of 10^1 to 10^2 years may be estimated using river sediment loads (Andermann et al., 2012), while depositional site studies or exhumation histories based on thermochronology may be associated to the long-term mass transfer over up to 10^6 years (e.g. Kirchner et al., 2001; von Blanckenburg, 2005). In the case of mountain areas, high discharge variability and the mainly local, short-term character of depositional sites complicate the assessment of representative erosion rates. Cosmogenic nuclide (CN) techniques allow to quantify erosion rates representative of the average conditions in upstream areas (e.g. Brown et al., 1995; Bierman and Steig, 1996; Granger et al., 1996; Schaller et al., 2001; von Blanckenburg, 2005; Dunai, 2010). The production of CN in the Earth's surface implies that the CN concentration of the material removed from the surface inversely scales to erosion (Lal, 1991; Cerling and Craig, 1994; Bierman and Steig, 1996; Granger et al., 1996; Gosse and Phillips, 2001; Dunai, 2010). Measuring the concentration of CN in

ESURFD
3, 83–128, 2015

fluvial sediments then allows to infer basin-wide erosion rates that integrate over time scales of 10^2–10^4 years and deliver a reference of the "natural background" erosion (e.g. Kirchner et al., 2001; von Blanckenburg, 2005).

In this study, we aim at determining the magnitude of erosion in Pamir at the millennial time-scale and at identifying the factors that explain its variability. We analyze eleven samples of fluvial sediments from the active channels of the Panj river network. The locations selected for sampling allow us to resolve the spatial variations of basin-wide erosion rates for all major sub-basins as well as record changes with increasing basin sizes along the trunk river. We measured the long-lived cosmogenic radionuclide ^{10}Be in the target mineral quartz by accelerator mass spectrometry at DREAMS (Akhmadaliev et al., 2013). For our calculation of production rates and shielding factors, we account for the topography of individual basins upstream of each sampling site. We apply a multiple linear regression analysis including geomorphic (altitude, relief, slope) and climatic (snow and ice cover, and precipitation) basin parameters to find the variables that explain variations in basin-wide erosion. Based on the best correlation and our own previous results, we discuss the variations of basin-wide erosion rates and the influence of spatial and temporal averaging. This contribution focusses on the first CN erosion rates measured in the Pamir and their implications for our understanding of surface processes in that region. This paper is a distinct addition to previous works (Fuchs et al., 2013, 2014) based on OSL dating of river terraces and geomorphic indicators that have shown the response of the Panj drainage system to tectonics, i.e. incision rate variability related to main tectonic structures in the Pamir and a possible reorganization of the Panj drainage system.

ESURFD
3, 83–128, 2015

2 Regional setting

2.1 Geological setting

The Pamir is located at the northwestern end of the India–Asia collision zone. The series of sutures, magmatic belts and crustal blocks are assumed to consist of along-strike equivalents of the Tibetan Plateau that accreted to the Eurasian plate during the Paleozoic to Mesozoic (e.g. Burtman and Molnar, 1993; Schwab et al., 2004; Cowgill, 2010; Bershaw et al., 2012). The main tectonic structures allow the distinction between three distinct terranes: the Northern, Central, and Southern Pamir (Burtman and Molnar, 1993; Schwab et al., 2004). The bulk of the Pamir comprises a steady-state elevated plateau of Cenozoic domes that cover up to 30 % of the Pamir (Ducea et al., 2003; Schwab et al., 2004; Schmidt et al., 2011; Stübner et al., 2013). The structural domes (Fig. 1a) expose Cretaceous arc-type granitoids, mantled by lower-grade to non-metamorphic rocks (Schwab et al., 2004; Robinson, 2009; Schmidt et al., 2011; Stübner et al., 2013). The northern Kurgovat Dome consists of high-grade metamorphosed Triassic rocks. The central Yazgulom, Sarez, Muskol, Shatput and the southern Shakhdara and Alichur Domes exhumed high-grade metamorphic rocks of Oligocene to Miocene ages with peak exhumation at ∼15 Myr (Schmidt et al., 2011; Stübner et al., 2013).

The active frontal range of Pamir bends nearly 180° from northern Afghanistan to western China (Bershaw et al., 2012). Neotectonic activity is governed by the northward propagation of the Indian plate inducing east–west striking mountain ranges. Crustal shortening is mainly accommodated at the Main Pamir Trust (MPT) by subduction beneath the frontal part of the orogen where most of the seismicity occurs (e.g. Koulakov and Sobolev, 2006; Schneider et al., 2013; Sippl et al., 2013). Recently published shortening rates reach 10–15 $mm\,yr^{-1}$ across the MPT (Ischuk et al., 2013). The lateral margins of the orocline display strike-slip motion of ∼12 $mm\,yr^{-1}$ along the western Darvaz Fault Zone (DFZ) (Trifonov, 1978; Mohadjer et al., 2010) and $< 1\,mm\,yr^{-1}$ along the eastern Karakoram Fault Zone (KFZ) (Strecker et al., 1995). The Southern

ESURFD
3, 83–128, 2015

Pamir Shear Zone (SPSZ) delineates the Pamir to the south from the Hindu Kush. This major east–west, low-angle normal fault comprises the southern boundary of the giant Shakhdara Dome. Plateau-internal neotectonic seismicity is related to the gravity driven collapse of the Plateau and the induced east–west extension and conjugated strike-slip (Fan et al., 1994; Strecker et al., 1995; Sippl et al., 2013).

2.2 Climatic setting

The setting of the Pamir at the transition between the Westerlies and the ISM makes the region highly sensitive to variations in atmospheric circulation patterns. Tropical Rainfall Measurement Mission (TRMM) spatial product 3B42 V7 (Huffman et al., 1997, 2007) reveals strong variations of annual precipitations (mean 1998–2012) from almost nil to more than 500 mm in Pamir (Fig. 1b). The Westerlies supply precipitation during winter and spring to the north-western Pamir margins. The precipitation from the south during the ISM strongly attenuates over the Hindu Kush and Karakoram Range. The central Pamir receives very little annual precipitation, mainly in form of snow. The westward increase of permanent snow and ice cover (Moderate Resolution Imaging Spectrometer, MCD12Q1, version 057, 2010, Strahler et al., 1999) illustrates the superimposition of concentrated precipitation at the Pamir margins and low temperature due to high altitudes (Fig. 1b).

The efficiency of glacial processes on erosion is highly debated (e.g. Norton et al., 2010; Godard et al., 2012), which, dependent on the averaging time of erosion rates, requires precise knowledge on temporal fluctuations of glacial extents. Glacial remnants attest for significant climatic variations during the Late Quaternary on the Pamir Plateau. Successively less extensive glacial advances correspond to an increasing aridity in Central Asia (Zech et al., 2005; Abramowski et al., 2006; Röhringer et al., 2012). Beryllium-10-based dating of moraines on the Pamir Plateau puts the most extensive glaciation during the marine isotope stage (MIS) 4 or earlier, during MIS 5 to MIS 6. The glaciers of this most extensive glacial advance reached the inner-plateau valley floors 136–93 and 86–60 kyr ago. A potential ISM driven MIS 3 advance related to hummocky moraines is ambiguous due to high age scatter. Two less extensive advances are dated at 30–27 kyr (MIS 3/MIS 2) and 24–22 kyr (MIS 2). Younger glacial sediments are associated to de-glaciation or minor re-advances.

3 Material and methods

3.1 Beryllium-10-based modern erosion rates

Beryllium-10 concentrations in modern fluvial sediments scale to the rate of landscape lowering by weathering and physical erosion and average the time of exposure to cosmic ray interaction in rock surfaces (von Blanckenburg, 2005; Dunai, 2010). The generally dry conditions in Pamir (Fig. 1) suggest weathering to be of less importance in the total erosion budget. In this case, landscape lowering is dominated by the physical material removal at the landscape's surface, which means that denudation rates narrow down to erosion rates (e.g. Dunai, 2010), and it may be convenient to use both terms interchangeably in the following.

The relation between the ^{10}Be concentration in a target mineral and modern erosion rates is based on the fact that the nuclide is produced by cosmic rays at rock surfaces within a rock-characteristic attenuation depth, while material removal brings constantly new material from shielded depth to the surface (Lal, 1991; Brown et al., 1995; von Blanckenburg, 2005; Dunai, 2010). Being highest at the rock surface, the ^{10}Be production decreases approximately exponentially with depth (Lal, 1991; Dunne et al., 1999; Braucher et al., 2011). The mean attenuation path length z^* of cosmic rays in rocks depends on the attenuation coefficient of the nucleonic component ($\sim 160\,\mathrm{g\,cm^{-2}}$) and the rock density (e.g. Gosse and Phillips, 2001; Balco et al., 2008) of the bulk, often polymineral material. Accordingly, in silicate rocks z^* is typically $\sim 60\,\mathrm{cm}$ (Lal, 1991; von Blanckenburg, 2005). The ^{10}Be concentration C is then proportional to the time the mineral grains reside within z^* until being removed from the surface. Consequently, C is inversely proportional to the erosion rate ε (Lal, 1991; Brown et al., 1995; von

ESURFD
3, 83–128, 2015

Blanckenburg, 2005). This relation can be described by:

$$\varepsilon = \left(\frac{P}{C} - \lambda\right) \cdot z^* \tag{1}$$

where λ is the decay constant of the nuclide and P its production rate. To calculate λ by

$$\lambda = \frac{\ln(2)}{t_{1/2}} \tag{2}$$

we used the ^{10}Be half-life ($t_{1/2}$) of (1.387 ± 0.012) Myr (Korschinek et al., 2010). The parameter z^* may be treated as a constant when determining basin-wide erosion rates that averages over local variations in rock densities affecting the attenuation path length. The central estimates required for solving the equation are the ^{10}Be concentration of the sample and the rate of nuclide production at the corresponding location (details given in Sects. 3.2, 3.3 and 3.4). The equation is valid under steady-state conditions of ^{10}Be production and material removal at the surface. This implies constant conditions over a period that is long compared to the averaging time T_{ave}, the time it takes to erode z^* and hence, to remove the "cosmogenic memory" of the material (Brown et al., 1995; Bierman and Steig, 1996; von Blanckenburg, 2005; Dunai, 2010).

Assuming uniform erodibility, mineral composition and grain size release of the eroding rock surface, erosion rates represent averages for all upstream surfaces at the basin scale (Bierman and Steig, 1996; von Blanckenburg, 2005; Carretier et al., 2009). Well-mixed sediment representative of all process domains within the basin require sample basins large enough to minimize the influence of single and only local processes (e.g. von Blanckenburg, 2005). Although large basins imply longer grain travel times, nuclide concentrations revealed negligible increases compared to the concentration already acquired at their initial position in non-aggrading basins (Carretier et al., 2009).

ESURFD
3, 83–128, 2015

3.2 Sampling strategy

We sampled 11 locations of the Panj river network (Fig. 1b). Five sampling sites represent the increasing basin along the trunk river reach of the Panj until it crosses the DFZ. Three major tributaries (Gunt, Bartang and Vanj River, Fig. 1b) were sampled near their confluence with the Panj and three additional sites were selected to represent upstream sub-basins. Difficulties to find suitable sites of modern fluvial sediments arose from the high stream power of the Panj that limits the deposition of sand in Pamir.

To ensure complete mixing of sediment grains that are representative for all upstream source areas, we chose locations before confluences as far as possible from upstream tributaries. Locations have been avoided where slope failure or fan sedimentation from minor tributaries indicated local perturbations. We sampled directly the uppermost 1–3 cm of the sediment in the active river channel. All samples consisted of predominantly sand-sized, quartz-rich polymineral material. Sufficient material for quartz and subsequent ^{10}Be extraction was addressed by collecting 3–5 kg of fluvial sediment per sample.

3.3 Sample preparation and ^{10}Be measurements

The polymineral sediment samples required quartz enrichment before starting chemical cleaning and ^{10}Be extraction. To narrow the grain size fraction, we first sieved the samples to 250–500 and 500–1000 µm, and focussed on the 250–500 µm fraction. For two samples (TA28C and TA30P) only the coarser fraction yielded sufficient material. After magnetic separation and ultrasonic bath, we cleaned the quartz with a 1 : 1 solution of HCl (32 %) and H_2SiF_6 (34 %) (Brown et al., 1991). Inspection of the sample's mineral composition under the binocular revealed relatively high proportions of feldspars (up to 50 %) for most of our samples, even after repeating the partial dissolution for six cycles. Feldspars cause bias in quartz results due to differing rates of ^{10}Be production. Additionally, the lower chemical resistance compared to quartz as well as high aluminum contents affect chemical procedures. This motivated us to introduce a standard feldspar flotation (Herber, 1969) to further enrich the quartz fraction. The feldspar flotation was carried out in a solution of 0.2 % HF and pH of 2.4–2.7 to activate feldspar adherence to bubbles using the foam agent dodecylamine.

Atmospheric ^{10}Be was removed by dissolving 30 % of the extracted quartz fraction with 48 % HF during three cycles. The BeO separation followed the procedures by Merchel and Herpers (1999). After the addition of about 300 µg of a ^{9}Be carrier (Phena DD, $(3.025 \pm 0.009) \times 10^{-3}$ $^{9}Be\,g^{-1}$, Merchel et al., 2008), samples were totally dissolved using 48 % HF. The Be extraction from the dissolved quartz included repeated hydroxide precipitation by NH_{3aq}, anion and cation exchanges. For high Ti-containing samples, Ti was diminished by precipitation of $Ti(OH)_4$ before ignition of $Be(OH)_2$ to BeO. Then, target preparation involved adding Nb (six times of the dry oxide weight). AMS measurements were conducted at DREAMS (DREsden AMS, Helmholtz-Zentrum Dresden-Rossendorf, 6 MV, Cu cathode) using the in-house standard SMD-Be-12 (Akhmadaliev et al., 2013) normalized against the NIST SRM 4325 standard ($^{10}Be/^{9}Be$ ratio of $(2.79 \pm 0.03) \times 10^{-11}$, Nishiizumi et al., 2007). A round-robin exercise of AMS facilities confirmed robust standard calibration and measurement configuration (Merchel et al., 2012). Processing blanks were treated and measured parallel to the sediment samples. The blank isotope ratios in the order of 0.3–1.7 % ($^{10}Be/^{9}Be$ ratio of 2.0×10^{-15} and 2.1×10^{-15}) were subtracted from the measured ratios of all samples.

3.4 Production rates and shielding factor

The production of ^{10}Be in quartz is primarily dependent on the cosmogenic particle flux from nucleons and muons (Lal, 1991; Granger and Muzikar, 2001) as a function of the geomagnetic field, altitude and shielding (Lal, 1991; Brown et al., 1995; Bierman and Steig, 1996; Stone, 2000; Gosse and Phillips, 2001). Accounting for the location-specific modulation, reference sea level and high latitude (SLHL) production rates need to be scaled to the conditions at the site of sampling. In the case of fluvial sediment samples, the cosmogenic nuclide inventory was acquired in source areas of the sediment upstream of the sampled site (e.g. Brown et al., 1995; Bierman and Steig, 1996; Granger et al., 1996; von Blanckenburg, 2005). Consequently, the calculation of representative production rates requires attention to the hypsometry of the whole basin (von Blanckenburg, 2005; Norton and Vanacker, 2009; Dunai, 2010).

Representative values for the ^{10}Be production rate and shielding of individual sample basins requires the identification of the upstream area for each sampling site. The drainage area calculation included basic data processing of a ASTER GDEM of 30 m resolution (NASA Land Processes Distributed Active Archive Center) for flow directions, accumulation area and stream segments (QGIS Development Team, 2010; GRASS Development Team, 2012). Assuming total shielding by permanent ice and snow cover, we excluded respective areas from further calculations of ^{10}Be production rates. The areas of permanent snow and ice cover are based on MODIS (Moderate Resolution Imaging Spectrometer) Land Cover Type data MCD12Q1 (Strahler et al., 1999) and the classification scheme according to the IGBP (International Geosphere Biosphere Programm). The available data covers the years 2000–2012. For our calculations, we use the year 2010 that is among those with most extensive snow and ice cover. The area upstream of the Lake Yashilkul was not included into basin analyses as a large landslide dams the plateau discharge and sediment flux. The dam is assumed to have been in place for several 10^4 years (Zech et al., 2005; Brookfield, 2008).

For each sampled basin, we then calculated ^{10}Be production rates from neutrons, and fast and stopped muons by raster cell-resolved scaling of a SLHL reference according to Stone (2000). We used the SLHL production rate of 4.5 at g^{-1} quartz yr^{-1} (cf. Balcoet al., 2008, along with the half-life of ^{10}Be of $(1.387 \pm 0.012) \times 10^6$ years, Korschinek et al., 2010) and the attenuation parameters according to Braucher et al. (2003) and Siame et al. (2004).

Topographic shielding plays an important role in high relief terrain (Dunne et al., 1999) as steep slopes reduce the exposure to the cosmic particle flux (e.g. Gosse and Phillips, 2001; Codilean, 2006; Norton and Vanacker, 2009). Shielding from other sources is considered negligible as glaciated areas are excluded from production rate

ESURFD

3, 83–128, 2015

calculation and vegetation is scarce due to the dry climate and high basin altitudes. The shielding factor was estimated for each GDEM raster cell based on the horizon line within a 10 km distance according to the method of Codilean (2006). Norton and Vanacker (2009) found only low underestimation of shielding when using a DEM of 30 m resolution in steep terrain.

The raster-cell resolved production rates and shielding factors of each sampled basin show non-normal, skewed to poly-modal distributions due to topographic variations. We use the arithmetic mean to represent the conditions within the basins. Uncertainties are calculated based on the standard deviation to refer to high variability of values within basins. The uncertainties of erosion rates refer to the sum of errors from AMS measurements of the ^{10}Be concentration, and the variation of production rates and shielding.

3.5 Sample basin parameters

Basin-wide denudation rates have been found to correlate with altitude, slope, relief, precipitation or glaciated area (e.g. Schaller et al., 2001; Montgomery and Brandon, 2002; von Blanckenburg, 2005; Norton et al., 2010). We describe the sampled basins in Pamir by probability density estimates of altitude, slope and precipitation (TRMM product 3B42 V7) using the R programming environment (R Core Team, 2013). The median, 0.25 and 0.75 quartiles of each parameter serve for (multiple-) linear regression analyses to infer the importance of individual parameters for explaining the variations in erosion. We examine the influence of glacial processes using the proportion of permanent snow and ice cover in sampled basins. From the MODIS data of the year 2010 (see above), we calculate the area covered by snow and ice proportional to the basin size.

We characterize the relief of each sample basin using the altitude difference at different scales. The basin relief determines the overall altitude difference within sampled basins. We calculate the basin relief using the difference between the 0.75 and 0.25 quartiles of basin altitudes, to compensate for the bias towards highest relief for largest

ESURFD
3, 83–128, 2015

basins. The local relief represents altitude differences normalized to a given area. We use a moving window of 1 and 4 km width to analyze the GDEM data and determine the relation between relief and erosion at the sub-basin scale. A smaller window size narrows relief estimates down to slope, a wider window size reproduces trends of basin relief.

4 Results

4.1 Sample basin properties

The basins of the southern Panj and of the major Panj tributaries show strong east–west elongations (Fig. 1b). The basin elongation allow to integrate gradients from the Pamir Plateau to its western margin, while their parallel configuration enables to resolve south–north changes in controlling factors. The trunk reach connects tributary outlets from south to north close to the western drainage divide of the entire investigated Panj basin. The median basin altitudes gently decrease from 4800 to 4200 m a.s.l. along the course of the Panj (cf. Fig. 1). The minimum altitudes representing the river bed sharply drop from 3600 to 700 m a.s.l. (Table 1) and reveal the downstream (northward) increase in total altitude differences for larger basins. The strong decrease of minimum altitudes witnesses strong incision at the Pamir margins.

On the plateau, altitudes cluster between 3800 and 5000 m a.s.l. with significantly less frequent lower altitudes (Fig. 2a, bottom panel). The basins of the southern Panj are slightly higher compared to those at the western Pamir margin. A strong drop in altitude frequencies delineates the Pamir Plateau from its margins (Fig. 2a). The main frequency contrast occurs at ~ 3800 m a.s.l. at the southern Pamir margin and less sharply at ~ 3600 m a.s.l. at the the western margin. Two minor peaks at ~ 3300 and ~ 2800 m a.s.l. indicate local base levels below the Pamir Plateau (cf. Fig. 2a, top panel) in the southern Panj basins. The local base levels are masked in western Pamir basins

ESURFD
3, 83–128, 2015

by the increasing basin size. The Vanj basin (TA02A) stands out by its high proportion of margin-related altitudes indicating low influence from plateau-related areas.

The relative proportions of slopes within basins correspond to respective altitude distributions. Highly variable slopes display strongly bimodal distributions in the east–west elongated basins that range over plateau and marginal basin portions (Fig. 2b, middle panel). The narrow peak of slope frequencies below 5° scales with the plateau-related, very flat basin portions between 4000 m and 5000 m a.s.l. (cf. upper Bartang, TA08N, Fig. 2b, bottom panel). Such areas are less extensive in the southern Panj basins that contour the Pamir at its southern margin Fig. 2b, top panel). The second, much broader frequency peak indicates hillslopes to cluster at roughly 35°. The Vanj basin (TA02A, Fig. 2, center panel) stands out with a negatively skewed slope distribution and maximum frequencies at ~ 40°. Although draining the Plateau, the Shakhdara basin (TA30P, Fig. 2b, bottom panel) displays a broad slope distribution with a plateau of high frequencies between 10 and 30° that suggests a transient position of the basin located on the edge of Pamir Plateau.

Areas of permanent ice and snow cover reflect the predominant moisture supply from the northwest and south, and evidence the aridity of the central-eastern parts of Pamir (Fig. 1b). The Pamir basins are very heterogeneously affected by ice and snow. The largest coverage of permanent ice and snow cover show the small basin of an upper Panj (Pamir River) tributary (TA23P, 55 %) and the northernmost basin of the Vanj River (TA02A, 37 %). In contrast, only 5 % of the upper Bartang (TA08N) basin at the eastern plateau are permanently covered by snow and ice (Table 1). A similar picture can be drawn from the median of TRMM-based mean annual precipitation (1998–2012). The largest basins TA23A and TA08B indicate an regional average of ~ 300 mm yr^{-1}. Variations in precipitation are mainly controlled by orographic gradients of the predominant atmospheric circulations.

ESURFD
3, 83–128, 2015

4.2 Erosion rate parameters

The ^{10}Be concentrations show a high variability between sample basins (Table 2). Nuclide concentrations are comparable ($5.7–7.6 \times 10^4$ at g^{-1}) along the Panj and do not show any trend from upstream, smaller basins towards downstream basins of largest size. The tributary basins display a northward decrease in concentrations (TA31B, TA01C, TA02A) but the east–west elongated basins cause averaging of plateau-related and marginal basin portions. Especially concentrations measured for the Bartang basin (TA01C) is affected by including the upstream basin (TA08N) of highest ^{10}Be concentrations of $(98.5 \pm 2.1) \times 10^4$ at g^{-1}, while the downstream basin portion can be assumed to contribute very low concentrations to the sediment mix. Similarly, the Gunt basin (TA31B) comprises also the conditions in the Shakhdara River sub-basin (TA30P) that has two times the concentration found in the entire Gunt basin. The Vanj basin (TA02A) yields the lowest concentration with $(1.9 \pm 0.1) \times 10^4$ at g^{-1}.

Estimated production rates of ^{10}Be (cf. ^{10}Be production rates due to neutrons in Fig. 3, top panel) correspond to the basin topography with one prominent maximum at ~ 80 at g^{-1} yr^{-1}. Increased altitude variations at the western Pamir margin cause skewed distributions. Excluding areas covered by snow and ice lowers production rates in systematic manner, modulated by the amount of precipitation (Fig. 4a). The limited snow and ice coverage at the eastern plateau affects production rates less compared to the more extensive coverage in the northwestern marginal basins. The high proportion of snow and ice covered areas in north-western Pamir basins implies discarding mainly high elevated areas prone to high production rates as most evident for the Vanj basin (TA02A). The effect amounts to less than 10 % for all sample basins but TA23P and TA02A with up to 20 % lower values. Erosion rates corrected for the basins proportion of snow and ice cover display an exponential relation with AMS-based ^{10}Be concentrations (Fig. 4b) as an expression of the attenuation of cosmic rays in rock surfaces.

ESURFD
3, 83–128, 2015

Topographic shielding factors range from roughly 0.8 to 1.0 with a narrow and a wide maximum in frequencies (Fig. 3, bottom panel) that mimic the distribution of slopes. The correction of production rates according to the basin's topographic shielding factors enhance differences between basins. Low altitude areas commonly relate to marginal Pamir basins that are more shielded by steep slopes than plateau-related basins with a high proportion of altitudes above 3600 m a.s.l. and large areas of slopes < 5 %. Consequently, elevated central and eastern basin portions deliver sediments of high ^{10}Be concentrations (e.g. TA08N) to the river channels due to high production and low shielding. Lowest production rates occur within north-western basins (e.g. TA02A) due to both, high topographic shielding and high snow and ice cover. The rates of nuclide production (Table 2) are similar, with only ∼ 9 % variability for plateau-related basins (TA08N and TA30P) and those of the southern Panj basins (TA23P, TA24O, TA25C and TA28C). The shielding corrected production rates in tributary basins indicate a slight decrease (Fig. 4c) corresponding to northward lower altitudes and steepened topography.

4.3 Basin-wide erosion rates

The two largest basins (TA23A and TA08B) reveal an high average erosion for the entire Pamir with ∼ 0.64 mm yr^{-1} (Fig. 5). Erosion rates determined along the Panj resemble the average conditions and stay relatively consistent despite significant changes in basin sizes. Minor variations indicate a slight, westward decrease in erosion with increasing size of the southern Panj basins. The erosion rate of (0.79 ± 0.19) mm yr^{-1} for the eastern, upper Panj (TA23P, small Pamir River tributary) lowers to (0.58 ± 0.18) mm yr^{-1} for the entire southern Panj basin before the river course deflects to the north. The erosion rates rapidly increases downstream to (0.74 ± 0.24) mm yr^{-1} despite a relatively modest increase of drainage (∼ 13 %).

The major tributaries of the Panj (Gunt, Bartang, Vanj) reveal strong contrasts in erosion across the Pamir ranging from (0.05 ± 0.01) to (1.45 ± 0.56) mm yr^{-1} (Table 2). The pattern of erosion illustrates increasing rates from the south-eastern central plateau to-

ESURFD
3, 83–128, 2015

wards the north-western margins. Two upstream sub-basins determine low erosion on the Pamir Plateau with (0.05 ± 0.01) mm yr^{-1} for the easternmost inner plateau (TA08N) and (0.16 ± 0.05) mm yr^{-1} for the south-western Shakhdara basin (TA30P). The morphometry of those plateau-related areas is characterized by the predominance of altitudes above 3600 m a.s.l. and large areas of slopes below 5° (cf. Table 2). Erosion rates determined immediately before the confluence with the Panj show a northward increase from ~ 0.37 to 1.45 mm yr^{-1} in major tributary basins (Gunt, Bartang, Vanj). Rates of the elongated Gunt (TA31B) and Bartang (TA01C) basins integrate the low erosion of upstream plateau-related sub-basins (TA08N and TA30P). Consequently, erosion in downstream basin portions across the Pamir margin lies above the basin-wide average. The differentiation of high erosion in marginal sub-basins fits to the erosion rate of (1.45 ± 0.56) mm yr^{-1} for the Vanj basin (TA02A) that reflects conditions at the northwestern Pamir margin without significant portions of the typically flat, plateau-related basins.

We estimate the erosion rates of the lower portions of the Gunt (GUNT) and the Bartang (BARlow) by relating rates of the upstream basin area for which we have data to those of the entire basins. We scaled the erosion rates by their relative area as a simple approximation. The average erosion rate for the entire basin ($\varepsilon_{\text{total}}$) represents the sum of area-weighted erosion rates in its upper and lower sub-basins (up and down) by

$$\varepsilon_{\text{total}} = a \cdot \varepsilon_{\text{up}} + (1 - a) \cdot \varepsilon_{\text{down}}. \quad (3)$$

The area factor a (normalized to 1) describes the portion of the upstream sub-basin relative to the area of the entire basin. The approach yields area-weighted erosion rates of 0.53 mm yr^{-1} (GUNT) and 1.64 mm yr^{-1} (BARlow) for downstream basin portions ($\varepsilon_{\text{down}}$, Table 3). Applying the same approach to the southern Panj basins enhances the contrast in erosion where the southern Panj deflects to the north at the western Pamir margin. The relative areas of the basin TA24O and TA25C indicate an erosion rate of only 0.02 mm yr^{-1} for the inferred sub-basin ISHs. In contrast, the inferred sub-basin

Discussion Paper | Discussion Paper | Discussion Paper | Discussion Paper |
ESURFD
3, 83–128, 2015
Millennial erosion rates across the Pamir dominated by topographic factors
M. C. Fuchs et al.

between TA25C and TA28C (ISHn) suggests a very high erosion rate of 1.81 mm yr^{-1}, comparable to those of the lower Bartang basin (BARlow) and the Vanj basin (TA02A). However, the area-weighted erosion rates may be biased as the actual contribution of individual basin portions to the sampled mix of material remains unresolved.

The area factor a can be replaced by a slope factor s to account for morphometric differences in basin portions. The factor s describes the ratio of the sub-basin slope scaled the slope of the entire basin and normalized to 1 (i.e. division by 2 in the case of two basins). Slope-weighted erosion rates are then determined by using the Eq. (3). Inferred rates indicate an improved fit to morphometric units and respective trends in basin-wide rates of measurement data. The slope-weighted erosion rates are 0.54 mm yr^{-1} for the sub-basin GUNT, 1.23 mm yr^{-1} for BARlow, 0.46 mm yr^{-1} for ISHs and 0.89 mm yr^{-1} for ISHn (Table 3).

4.4 Relationship between erosion rates and basin parameters

Linear regression analyses deliver a simple, straightforward evaluation of basin characteristics. The absence of any trend with increasing basin size suggests no significant nuclide acquisition during grain transit through the basin. Results reveal a primary role of topographic basin parameters on variations of erosion rates (Fig. 6). The basin-wide erosion rates are proportional to altitude difference within basins, but highlight the scale-dependent relation between relief estimates and erosion rates. The basin relief (BR, Fig. 6a) shows no correlation, while reducing the window size of the local relief (LR, Fig. 6a) to 1 km yields an R^2 of 0.68. The highest correlation to erosion rates is attained with basin slopes. Using the median slopes yields an R^2 of 0.73 and the 0.75 quartiles an R^2 of 0.81 (Fig. 6b). The correlation of erosion with slopes suggests that the slope-weighted erosion rates for the inferred sub-basins GUNT, BARlow, ISHs and ISHn suite the primary relationship found in regression analyses (Table 3).

The variations in mean annual rainfall between 270 and 380 mm (based on TRMM rainfall data) cannot explain the pattern of erosion (R^2 of < 0.1). Similar basin erosion

ESURFD
3, 83–128, 2015

rates cluster regardless of low or high precipitation, although high erosion relates to basins receiving highest annual precipitation. The limited influence of precipitation on erosion may relate to the overall low precipitation, predominantly in form of snow and temperature induced peak discharge in the melting season. The relative area covered by snow and ice shows no strong relation to erosion rates with an R^2 of < 0.4.

We performed a multiple linear regression analysis with two components as predictors for erosion. Including more components result in multi-collinearity and insignificant effects on the goodness of correlation. The best results were obtained by combining the 0.75 quartiles of slope and TRMM data with a R^2 of 0.93 (Fig. 6c). The regression with slope and TRMM rainfall data indicates that low slopes imply low erosion despite variations in precipitation, while high rainfall contributes to high erosion rates in the case of steep slopes. All other parameter combinations yielded lower correlations.

5 Discussion

5.1 Averaging times of Pamir erosion rates

For a robust interpretation of the Pamir erosion rates, it is important to consider the scales of averaging in terms of time and space. As stated above, the ^{10}Be-based erosion rates average over the time interval needed to erode the characteristic attenuation depth of about 60 cm. The erosion rates in Pamir average over time scales of 10^2 to 10^4 years i.e. the Holocene (Table 2). The high erosion rates for most of the Pamir basins imply a T_{ave} of less than 10^3 years. Such short time intervals for the renewal of the nuclide inventory suggest that the erosion rates represent modern conditions. Although the climate likely underwent fluctuations, there is no evidence for major changes during that time in glacial records (Zech et al., 2005; Abramowski et al., 2006; Röhringer et al., 2012). The moderate erosion rates (about 0.16–0.37 mm yr^{-1}) calculated for the Gunt (TA31B) and the Shakhdara basins (TA30P) average over the time since the middle/late Holocene. Only the eastern Pamir Plateau basin (TA08N) has

ESURFD
3, 83–128, 2015

a significantly longer T_{ave} averaging erosion over the time since the MIS 2–MIS 1 transition (Table 2). Changes in conditions during this period are likely but the large areas of low slopes formed by sediment-filled valleys of the inner Pamir are indicative of low erosion persistent over long time scales. However, the estimated T_{ave} means that variations in the absolute extent of glaciated areas are possible. T_{ave} is largely longer than the period covered by available MODIS data on permanent snow and ice disribution- and mostly to short to be resolved by glacial chronologies at the Pamir Plateau. We assume persistent climatic circulations and dry conditions during the last 10^3 with only slightly more extensive glaciations compared to today.

Another point to consider in terms of time scales is the nuclide built-up during grain transport from the source rock to the sampled site. Robust cosmogenic nuclide-derived erosion rates require that grain travel time through the sampled basin should be short compared to T_{ave} (Granger et al., 1996; von Blanckenburg, 2005; Dunai, 2010). A significant nuclide built-up would result in a downstream increase of ^{10}Be concentrations (Schaller et al., 2001), which is not indicated along the Panj. Concentrated discharge during the melting season and also the generally high slopes especially in marginal downstream basin portions suggest that sediment is annually transported over long distances. Only valleys in the plateau-related basins contain significant sediment fills witnessing relatively long storage periods. Nevertheless, this is in agreement with determined erosion rates.

Millennial scale ^{10}Be-based erosion rates in tectonically active landscapes such as the Pamir can be dependent on the magnitude-frequency distribution of mass wasting (e.g. Wolman and Miller, 1960; Korup et al., 2010; Korup, 2012; Lupker et al., 2012). High-magnitude low-frequency events may not be captured by millennial scale erosion rates. Their high effects on sediment delivery to river channel decrease fast within time intervals at decadal scale or longer (Wolman and Miller, 1960; Korup, 2012). The low abundance of such events in the study area (e.g. Lake Yashilkul) indicates their minor relevance.

ESURFD
3, 83–128, 2015

On the 10^6 year time scale, Stübner et al. (2013) estimated syn- to post-tectonic erosion rates of 0.3–0.5 mm yr^{-1} for the southern Pamir Shakhdara Dome and 0.1–0.3 mm yr^{-1} between the Shakhdara and Alichur Dome based on geometric constraints. These long-term estimates agree to the cosmogenic nuclide-based erosion rates of the same area. The higher rates fit to the marginal conditions of the Gunt basin, while the lower rates agree to conditions related to the inner southern Pamir (Skakhdara basin). The agreement suggests long-term persistence of erosion over time scales of 10^4 to 10^6. The erosion rates of < 0.5 mm yr^{-1} are low compared to the Pamir average and most other Panj as well as tributary basins. This delineates areas with long-term steady-state on the plateau of Pamir from marginal basins undergoing a transient stage with higher erosion rates of ~ 0.7 at a millennia scale. Erosion rates from river load gauging are not available yet, but may greatly differ from the ^{10}Be-based rates due to the mostly decadal period of records that imply dependence on the frequency of high-magnitude event and hillslope–river channel connectivity.

5.2 Spatial variations in erosion rates

The basin-wide erosion rates represent average values for their upstream areas. They may be biased in tectonic active landscapes when certain basin portions deliver unproportionally high amounts of sediments to the river channels, for example in form of landslides (e.g. Granger et al., 1996; von Blanckenburg, 2005; Dunai, 2010). For our samples, most basins are large enough to average effects of single basin portions and sampling sites are distant from major landslides or debris flows (e.g. the debris flow damming the Lake Yashilkul). Besides, they also average over differences in the erodibility and quartz abundance of rock types. However, the sediment release from individual geomorphic units within sample basins is certainly not uniform. Hence, small scale in situ data are needed to bridge this lack for a more detailed resolution of erosional domains within the studied Pamir basins. In particular, the sediment delivery from glaciated areas requires attention. Such areas contribute sediments that likely experienced negligible ^{10}Be productions rates. Excluding glaciated areas (Fig. 6a) lowers the production rates on the basin scale but this may be insufficient in the case of large quantities of glacial sediments in the sampled material.

The average erosion rates of basins along the Panj outline an overall agreement with the Pamir average of $\sim 0.64\,\mathrm{mm\,yr^{-1}}$ without any clear trend from smaller to larger basins (Fig. 5). In contrast, the studied tributaries reveal strong spatial variations in erosion. The major tributary basins indicate increasing erosion to the northwest. The east–west elongation of the tributary basins cause averaging across the plateau and its margins, while the Vanj basin (TA02A) is de-coupled from the plateau. The slope-weighted calculation of erosion rates enables to differentiate between conditions according to morphometry that are averaged by rates of the entire Gunt (TA31B) and Bartang basins (TA01C). This confirms upper sub-basins with very low erosion (about 0.05–$0.16\,\mathrm{mm\,yr^{-1}}$) in plateau-related regions and higher rates (about 0.54–$1.45\,\mathrm{mm\,yr^{-1}}$) in the lower marginal sub-basins.

Overall, the ^{10}Be-based basin-wide erosion rates are 10 times lower than OSL-based incision rates. Those incision rates cover the last major deglaciation period (the last 26 kyr, Fuchs et al., 2014), but indicate dominant control from local rather than temporal factors. The discrepancy between rates implies that the basin-wide erosion does not balance the lowering of the local base levels induced by the intense fluvial incision of the Panj at the Pamir margins. Despite the difference in magnitude, the spatial pattern agrees between fluvial incision along the Panj river profile and variations in erosion rates (Fig. 7). The decreased erosion rate of $(0.58 \pm 0.18)\,\mathrm{mm\,yr^{-1}}$ for the whole southern Panj basin (TA25C) and abrupt increase to $(0.74 \pm 0.24)\,\mathrm{mm\,yr^{-1}}$ agrees to intensified fluvial incision of 7–$10\,\mathrm{mm\,yr^{-1}}$, where the Panj turns to the north cutting across the Shakhdara Dome (Fig. 7; Fuchs et al., 2013, 2014). The change in process rates corresponds to morphometric evidence given by valley shape ratios (VSR), Hack Indices and riverbed convexity. The slope-weighted estimates (ISHs and ISHn) enhance the contrast in erosion by an increase from (0.46 ± 0.15) to $(0.89 \pm 0.28)\,\mathrm{mm\,yr^{-1}}$ and suggest a better representation of the local morphometric conditions as respec-

ESURFD

3, 83–128, 2015

Millennial erosion rates across the Pamir dominated by topographic factors

M. C. Fuchs et al.

tive estimates do not average over the entire upstream area. Lower erosion rates of (0.37 ± 0.11) mm yr^{-1} for the entire Gunt basin (TA31B) coincide with lower incision rates determined north of the confluence with the Gunt River where the Panj develops a more graded river profile (Fig. 7). Further north, average erosion rates of the Bartang (TA01C) and Vanj basins (TA02A) increase from 0.83 to 1.45 mm yr^{-1}. This trend is not resolved in OSL-based incision rates that vary between 4 and 6 mm yr^{-1} and are, on the relative scale, better comparable to the Pamir-wide average erosion rates of ~ 0.64 mm yr^{-1}. The de-coupling of the trends in erosion rates of northern tributary basins from the incision may relate to the already large Panj basin that becomes less sensitive to signals recorded by smaller tributary basins.

The magnitude of erosion is comparable with rates determined across the steep escarpment of the Himalaya (e.g. Godard et al., 2010; Andermann et al., 2012; Burbank et al., 2012; Lupker et al., 2012; Scherler et al., 2014), although conditions are different in Pamir. The monsoon-controlled southern flank of the Himalaya receives precipitation of up to 4 m yr^{-1}, where erosion rates exceed 2 mm yr^{-1}, while rates lower to ~ 0.1 mm yr^{-1} in the northern rain shadow of the Higher Himalayan and Tibetan Plateau (Burbank et al., 2012). Gabet et al. (2008) correlated erosion based on sediment flux in Nepal rivers to average monsoon precipitation with an R^2 of ~ 0.9. The sediment flux broadly scales with discharge. Suspended load data shows sediment flux dependent on the magnitude-frequency distribution of rainfall such that sediment pulses require an initial amount of precipitation (Andermann et al., 2012; Burbank et al., 2012). Andermann et al. (2012) emphasize the role of intense precipitation on generating direct runoff and sediment supply from hillslopes. The temperature-sensitive discharge in the high elevated northern rain shadow modulates the relation by peak discharge during the melting season. The hysteresis of sediment load and discharge suggests a supply limited behavior (Andermann et al., 2012; Burbank et al., 2012). Godard et al. (2014) describe a strong increase in erosion from 0.5–1 mm yr^{-1} in the Lesser Himalaya to 2–3 mm yr^{-1} in the Greater Himalaya despite relatively similar precipitation rates (R^2 of 0.13). They suggest erosion adapting fast to climatic changes and infer first-order

ESURFD
3, 83–128, 2015

control from large-scale tectonic uplift rates (R^2 of 0.78). The control of tectonic uplift on long-term erosion ($\sim 10^5$ years, based on thermochronology) agrees in uniform rates across the Greater Himalaya despite a fivefold increase in precipitation (Burbank et al., 2003). A primary control of tectonic-driven topographic steepness on erosion suggests that changes in precipitation are balanced by complex interactions between channel steepness and width, and concentrated sediment transport (Burbank et al., 2003; Scherler et al., 2014).

Steep slopes are also the primary factor controlling erosion in Pamir (R^2 of 0.81). Low erosion rates of $< 0.2\,\mathrm{mm\,yr^{-1}}$ are linked to the high-elevated, low-relief inner-plateau areas that are basically comprise the Cenozoic domes of the southern, central and eastern Pamir. At the Pamir margins, rapid base level lowering by the Panj facilitates steep slopes. But the high erosion rates of 0.54–1.45 $\mathrm{mm\,yr^{-1}}$ in marginal basin do not balance the fast incision driven by river captures across the Pamir domes (Fuchs et al., 2014). Highest rates coincide with increased precipitation at the north-western Pamir margin and suggest complex links between erosion, slopes and precipitation. Although precipitation alone does not reveal any correlation to erosion rates (R^2 of < 0.1), combined with the parameter slope multiple regression analyses yields a strong relationship by R^2 of 0.93. This multiple relation shows that steep slopes are the important precondition for the efficiency of precipitation for triggering erosion. In the overall dry Pamir, precipitation is a limiting factor for high erosion rates. Basins of highest erosion receive precipitation mainly in winter in form of snow that causes a temperature-sensitive concentration of discharge during the melting season. Less precipitation at the southern Pamir margins reduces the efficiency of sediment transport from hillslopes and out of basins. Consequently, basin-wide erosion cannot adjust to the high fluvial incision. Steep slopes as the first order control persist at the Pamir margins due to rapid, river capture controlled incision, but require sufficient precipitation for efficient sediment flux from hillslopes to the river channels. The lowest discrepancy between hillslope processes and fluvial incision is then reached in the north-western Pamir where sufficient

ESURFD
3, 83–128, 2015

winter precipitation causes seasonal peak discharge and drives the sediment flux out of basins.

6 Conclusions

The millenial, basin-wide erosion rates of ~ 0.64 mm yr^{-1} for the entire Pamir highlight a rapid landscape evolution. This regional-scale erosion averages over very different morphometric units of the orogen. Individual sub-basins of the major tributaries emphasize strong contrasts in erosion between the Pamir margins (0.54 to 1.45 mm yr^{-1}) and the inner plateau (0.05 to 0.16 mm yr^{-1}). The pattern of erosion reveals fast material removal related to high variations in altitude and local base levels at the margins, and much longer residence of material where large flat areas define the constant local base level of the Pamir Plateau.

Topography affects erosion rates in Pamir especially through the prevalence of steep slopes (0.75 quartiles) that explain about 80 % of the variations in erosion (R^2 of 0.81). The persistence of steep slopes implies either tectonic uplift or base level lowering. The steep slopes drive fast material supply to the river channels. Maintaining the steep slopes and related sediment flux largely depends on the capacity of rivers to transport the sediment out of the basins. Consequently, this also could indicate a climatic component affecting the river discharge.

Highest erosion rates at the Pamir margin coincide spatially with orographic precipitation delivered by the Westerlies, but our estimated erosion rates show no correlation to mean annual precipitation. The snow and ice coverage does not correlate (R^2 of < 0.4) with erosion. Multiple linear regression analyses with an R^2 of 0.93 outlines that steep slopes are an important precondition for the efficiency of erosion but also that a minimum of precipitation is required to allow the sediment transport in Pamir.

The water available for erosion shows high spatiotemporal variations (Pohl et al., 2014). It is largely controlled by the predominance of winter precipitation and its delayed release during the melting season. The resulting seasonal peak discharge during

ESURFD
3, 83–128, 2015

spring and early summer provides the condition for an effective sediment mobilization out of basins (Pohl et al., 2014) and hence, favors high erosion especially at the north-western Pamir margin. The drier Pamir Plateau does not generate sufficient discharge which results in the prevalence of low slopes corresponding to low erosion rates.

The magnitude of erosion is similar to rates determined across the south Himalayan escarpment and Tibetan Plateau (e.g. Godard et al., 2010; Andermann et al., 2012; Burbank et al., 2012; Lupker et al., 2012; Scherler et al., 2014), although both climatic and tectonic conditions are different in Pamir (e.g. Fuchs et al., 2013). In the Himalayas, a much higher amount of summer precipitation allows that the landscape adjusts faster to uplift conditions and fluvial processes compensate for variations in precipitation (e.g. Burbank et al., 2012). In the much drier Pamir, this adjustment is not reached. Incision clearly exceeds uplift. Basin-wide erosion rates do not balance the up to 10 times faster OSL-based incision rates measured along the Panj river (Fuchs et al., 2014). This significant discrepancy implies a transient landscape, for which precipitation is the limiting factor for hillslope adjustment to fluvial incision and for which we propose that river captures are responsible for the strong base level drop that drives incision along the Panj.

The limited coupling of erosion and incision has important implications on landscape evolution models and geohazard prediction (e.g. Gruber and Mergili, 2013). The dry conditions/low winter precipitation may limit the hillslope response to base level lowering to the close vicinity of the river channel itself, and hence, may intensify effects from hillslope length and channel network density. The strong incision and narrow wavelength of hillslope response suggest local relief steepening with increasing risks of sudden slope failures and resulting debris flows or landslides. Additionally, the case of the Pamir shows not only the complex interplay of tectonic and climatic factors, but highlights especially the importance of internal feedbacks in an evolving drainage system, here in form of river captures, that require implementation in landscape models.

Acknowledgements. We would like to thank the Department of Meteorology and Hydrology of Tajikistan for the support and organization during fieldwork in 2011. We are also grateful for the support of the DREAMS operator team facilitating AMS beam time, with special thanks to Shavkat Akhmadaliev, Stefan Pavetich and René Ziegenrücker. And we thank the DFG for funding our research associated with the TIPAGE project (GI362/4-1). We used GMT (Wessel, P. and W. H. F. Smith, New, improved version of the Generic Mapping Tools released, EOS Trans. AGU, 79, 579, 1998), QGIS (http://qgis.org/) and the R environment (http://www.r-project.org/) for most of the topographic data processing and the resulting figures. MODIS MCD12Q1 and ASTER GDEM data products were obtained through the online Data Pool at the NASA Land Processes Distributed Active Archive Center (LP DAAC), located at the US Geological Survey (USGS) Earth Resources Observation and Science (EROS) Center, Sioux Falls, South Dakota (https://lpdaac.usgs.gov/data_access).

References

Abramowski, U., Bergau, A., Seebach, D., Zech, R., Glaser, B., Sosin, P., Kubik, P. W., and Zech, W.: Pleistocene glaciations of Central Asia: results from ^{10}Be surface exposure ages of erratic boulders from the Pamir (Tajikistan), and the Alay–Turkestan range (Kyrgyzstan), Quaternary Sci. Rev., 25, 1080–1096, 2006. 90, 103

Akhmadaliev, S., Heller, R., Hanf, D., Rugel, G., and Merchel, S.: The new 6 MV AMS-facility DREAMS at Dresden, Nucl. Instrum. Meth. B, 294, 5–10, 2013. 88, 94

Andermann, C., Crave, A., Gloaguen, R., Davy, P., and Bonnet, S.: Connecting source and transport suspended sediments in the Nepal Himalayas, Earth Planet. Sc. Lett., 351–352, 158–170, 2012. 87, 107, 110

Balco, G., Stone, J. O., Lifton, N. A., and Dunai, T. J.: A complete and easily accessible means of calculating surface exposure ages or erosion rates from ^{10}Be and ^{26}Al measurements, Quat. Geochronol., 3, 174–195, 2008. 91

Bershaw, J., Garzione, C. N., Schoenbohm, L., Gehrels, G., and Tao, L.: Cenozoic evolution of the Pamir plateau based on stratigraphy, zircon provenance, and stable isotopes of foreland basin sediments at Oytag (Wuyitake) in the Tarim Basin (west China), J. Asian Earth Sci., 44, 136–148, 2012. 89

Bierman, P. R. and Steig, E. J.: Estimating rates of denudation using cosmogenic isotope abundances in sediment, Earth Surf. Proc. Land., 21, 125–139, 1996. 87, 92, 94, 95

ESURFD

3, 83–128, 2015

Bookhagen, B., Thiede, R. C., and Strecker, M. R.: Late Quaternary intensified monsoon phases control landscape evolution in the northwest Himalaya, Geology, 33, 149–152, 2005. 87

Braucher, R., Brown, E. T., Bourlès, D. L., and Colin, F.: In situ produced ^{10}Be measurements at great depths: implications for production rates by fast muons, Earth Planet. Sc. Lett., 211, 251–258, 2003. 95

Braucher, R., Merchel, S., Borgomano, J., and Bourlès, D. L.: Production of cosmogenic radionuclides at great depth: a multi element approach, Earth Planet. Sc. Lett., 309, 1–9, 2011. 91

Brookfield, M. E.: Evolution of the great river systems of southern Asia during the Cenozoic India–Asia collision: rivers draining north from the Pamir syntaxis, Geomorphology, 100, 296–311, 2008. 95

Brown, E. T., Edmond, J. M., Raisbeck, G. M., Yiou, F., Kurz, M. D., and Brook, E. J.: Examination of surface exposure ages of Antarctic moraines using in situ produced ^{10}Be and ^{26}Al, Geochim. Cosmochim. Acta, 55, 2269–2283, 1991. 93

Brown, E. T., Stallard, R. F., Larsen, M. C., Raisbeck, G. M., and Yiou, F.: Denudation rates determined from the accumulation of in situ-produced ^{10}Be in the Luquillo Experimental Forest, Puerto Rico, Earth Planet. Sc. Lett., 129, 193–202, 1995. 87, 91, 92, 94, 95

Burbank, D. W. and Anderson, R. S.: Tectonic Geomorphology, Blackwell Science, Wiley, 2000. 86

Burbank, D. W., Blythe, A. E., Putkonen, J., Pratt-Sitaula, B., Gabet, E., Oskin, M., Barros, A., and Ojha, T. P.: Decoupling of erosion and precipitation in the Himalayas, Nature, 426, 652–655, 2003. 86, 87, 108

Burbank, D. W., Bookhagen, B., Gabet, E. J., and Putkonen, J.: Modern climate and erosion in the Himalaya, C. R. Geosci., 344, 610–626, 2012. 87, 107, 110

Burtman, V. S. and Molnar, P.: Geological and physical evidence for deep subduction of continental crust beneath the Pamir, Geol. S. Am. S., 281, 1–76, 1993. 89

Carretier, S., Regard, V., and Soual, C.: Theoretical cosmogenic nuclide concentration in river bed load clasts: does it depend on clast size?, Quat. Geochronol., 4, 108–123, 2009. 92

Cerling, T. E. and Craig, H.: Geomorphology and in-situ cosmogenic isotopes, Annu. Rev. Earth Pl. Sc., 22, 273–317, 1994. 87

Champagnac, J.-D., Schlunegger, F., Norton, K., von Blanckenburg, F., Abbühl, L. M., and Schwab, M.: Erosion-driven uplift of the modern Central Alps, Tectonophysics, 474, 236–249, 2009. 86

Codilean, A. T.: Calculation of the cosmogenic nuclide production topographic shielding scaling factor for large areas using DEMs, Earth Surf. Proc. Land., 31, 785–794, 2006. 95, 96, 120

Cowgill, E.: Cenozoic right-slip faulting along the eastern margin of the Pamir salient, northwestern China, Geol. Soc. Am. Bull., 122, 145–161, 2010. 89

Ducea, M. N., Lutkov, V., Minaev, V., Hacker, B. R., Ratschbacher, L., Luffi, P., Schwab, M., Gehrels, G. E., McWilliams, M., Vervoort, J., and Metcalf, J.: Building the Pamirs: the view from the underside, Geology, 31, 849–852, 2003. 89

Dunai, T.: Cosmogenic Nuclides: Principles, Concepts and Applications in the Earth Surface Sciences, Cambridge University Press, Cambridge, 2010. 87, 91, 92, 95, 104, 105

Dunne, J., Elmore, D., and Muzikar, P.: Scaling factors for the rates of production of cosmogenic nuclides for geometric shielding and attenuation at depth on sloped surfaces, Geomorphology, 27, 3–11, 1999. 91, 95

Fan, G., Nil, J. F., and Wallace, T. C.: Active tectonics of the Pamir and Karakorum, J. Geophys. Res., 99, 7131–7160, 1994. 90

Fuchs, M. C., Gloaguen, R., and Pohl, E.: Tectonic and climatic forcing on the Panj river system during the Quaternary, Int. J. Earth Sci., 102, 1985–2003, 2013. 88, 106, 110, 128

Fuchs, M. C., Gloaguen, R., Krbetschek, M. R., and Szulc, A.: Rates of river incision across the main tectonic units of the Pamir identified using optically stimulated luminescence dating of fluvial terraces, Geomorphology, 216, 79–92, 2014. 88, 106, 108, 110, 128

Gabet, E., Burbank, D. W., Pratt-Sitaula, B., Putkonen, J., and Bookhagen, B.: Modern erosion rates in the High Himalayas of Nepal, Earth Planet. Sc. Lett., 267, 482–494, 2008. 86, 87, 107

Garzanti, E., Vezzoli, G., Andò, S., Lavé, J., Attal, M., France-Lanord, C., and DeCelles, P.: Quantifying sand provenance and erosion (Marsyandi River, Nepal Himalaya), Earth Planet. Sc. Lett., 258, 500–515, 2007. 87

Godard, V., Lavé, J., Carcaillet, J., Cattin, R., Bourlès, D., and Zhu, J.: Spatial distribution of denudation in Eastern Tibet and regressive erosion of plateau margins, Tectonophysics, 491, 253–274, 2010. 107, 110

Godard, V., Burbank, D. W., Bourlès, D. L., Bookhagen, B., Braucher, R., and Fisher, G. B.: Impact of glacial erosion on ^{10}Be concentrations in fluvial sediments of the Marsyandi catch-

ment, central Nepal, J. Geophys. Res., 117, F03013, doi:10.1029/2011JF002230 2012. 86, 87, 90
Godard, V., Bourlès, D. L., Spinabella, F., Burbank, D. W., Bookhagen, B., Fisher, G. B., Moulin, A., and Leanni, L.: Dominance of tectonics over climate in Himalayan denudation, Geology, 42, 243–246, 2014. 86, 87, 107
Gosse, J. C. and Phillips, F. M.: Terrestrial in situ cosmogenic nuclides: Theory and application, Quaternary Sci. Rev., 20, 1475–1560, 2001. 87, 91, 94, 95
Granger, D. E. and Muzikar, P. F.: Dating sediment burial with in situ-produced cosmogenic nuclides: theory, techniques, and limitations, Earth Planet. Sc. Lett., 188, 269–281, 2001. 94
Granger, D. E., Kirchner, J. W., and Finkel, R.: Spatial averaged long-term erosion rates measured from in situ-produced cosmogenic nuclides in alluvial sediment, J. Geol., 104, 249–257, 1996. 87, 95, 104, 105
GRASS Development Team: Geographic Resources Analysis Support System (GRASS GIS) Software, Open Source Geospatial Foundation, USA, available at: http://grass.osgeo.org (last access: 6 August 2014), 2012. 95
Gruber, F. E. and Mergili, M.: Regional-scale analysis of high-mountain multi-hazard and risk indicators in the Pamir (Tajikistan) with GRASS GIS, Nat. Hazards Earth Syst. Sci., 13, 2779–2796, doi:10.5194/nhess-13-2779-2013, 2013. 110
Herber, L. J.: Separation of feldspar from quartz by flotation, Am. Mineral., 54, 1212–1215, 1969. 94
Huffman, G. J., Adler, R. F., Arkin, P., Chang, A., Ferraro, R., Gruber, A., Janowiak, J., McNab, A., Rudolf, B., and Schneider, U.: The Global Precipitation Climatology Project (GPCP) combined precipitation dataset, B. Am. Meteorol. Soc., 78, 5–20, 1997. 90, 119, 122, 123
Huffman, G. J., Bolvin, D. T., Nelkin, E. J., Wolff, D. B., Adler, R. F., Gu, G., Hong, Y., Bowman, K. P., and Stocker, E. F.: The TRMM Multisatellite Precipitation Analysis (TMPA): quasi-global, multiyear, combined-sensor precipitation estimates at fine scales, J. Hydrometeorol., 8, 38–55, 2007. 90, 119, 122, 123
Huntington, K. W., Blythe, A. E., and Hodges, K. V.: Climate change and Late Pliocene acceleration of erosion in the Himalaya, Earth Planet. Sc. Lett., 252, 107–118, 2006. 86
Ischuk, A., Bendick, R., Rybin, A., Molnar, P., Khan, S. F., Kuzikov, S., Mohadjer, S., Saydullaev, U., Ilyasova, Z., Schelochkov, G., and Zubovich, A. V.: Kinematics of the Pamir and Hindu Kush regions from GPS geodesy, J. Geophys. Res.-Sol. Ea., 118, 2408–2416, 2013. 89

ESURFD
3, 83–128, 2015

Millennial erosion rates across the Pamir dominated by topographic factors

M. C. Fuchs et al.

Kirchner, J. W., Finkel, R. C., Riebe, C. S., Granger, D. E., Clayton, J. L., King, J. G., and Megahan, W. F.: Mountain erosion over 10 yr, 10 k.y., and 10 m.y. time scales, Geology, 29, 591–594, 2001. 87, 88

Korschinek, G., Bergmaier, A., Faestermann, T., Gerstmann, U. C., Knie, K., Rugel, G., Wallner, A., Dillmann, I., Dollinger, G., von Gostomski, C. L., Kossert, K., Maiti, M., Poutivtsev, M., and Remmert, A.: A new value for the half-life of ^{10}Be by heavy-ion elastic recoil detection and liquid scintillation counting, Nucl. Instrum. Meth. B, 268, 187–191, 2010. 92, 95

Korup, O.: Earth's portfolio of extreme sediment transport events, Earth-Sci. Rev., 112, 115–125, 2012. 104

Korup, O., Densmore, A. L., and Schlunegger, F.: The role of landslides in mountain range evolution, Geomorphology, 120, 77–90, 2010. 104

Koulakov, I. and Sobolev, S. V.: A tomographic image of Indian lithosphere break-off beneath the Pamir-Hindukush region, Geophys. J. Int., 164, 425–440, 2006. 89

Lal, D.: Cosmic ray labeling of erosion surfaces: in situ nuclide production rates and erosion models, Earth Planet. Sc. Lett., 104, 424–439, 1991. 87, 91, 94

Lupker, M., Blard, P.-H., Lavé, J., France-Lanord, C., Leanni, L., Puchol, N., Charreau, J., and Bourlès, D.: ^{10}Be-derived Himalayan denudation rates and sediment budgets in the Ganga basin, Earth Planet. Sc. Lett., 333–334, 146–156, 2012. 87, 104, 107, 110

Merchel, S. and Herpers, U.: An update on radiochemical separation techniques for the determination of long-lived radionuclides via accelerator mass spectrometry, Radiochim. Acta, 84, 215–219, 1999. 94

Merchel, S., Arnold, M., Aumaître, G., Benedetti, L., Bourlès, D. L., Braucher, R., Alfimov, V., Freeman, S. P. H. T., Steier, P., and Wallner, A.: Towards more precise ^{10}Be and ^{36}Cl data from measurements at the 10^{14} level: influence of sample preparation, Nucl. Instrum. Meth. B, 266, 4921–4926, 2008. 94

Merchel, S., Bremser, W., Akhmadaliev, S., Arnold, M., Aumaître, G., Bourlès, D. L., Braucher, R., Caffee, M., Christl, M., Fifield, L. K., Finkel, R. C., Freeman, S. P. H. T., Ruiz-Gómez, A., Kubik, P. W., Martschini, M., Rood, D. H., Tims, S. G., Wallner, A., Wilcken, K. M., and Xu, S.: Quality assurance in accelerator mass spectrometry: results from an international round-robin exercise for ^{10}Be, Nucl. Instrum. Meth. B, 289, 68–73, 2012. 94

Mohadjer, S., Bendick, R., Ischuk, A., Kuzikov, S., Kostuk, A., Saydullaev, U., Lodi, S., Kakar, D. M., Wasy, A., Khan, M. A., Molnar, P., Bilham, R., and Zubovich, A. V.: Partitioning

ESURFD

3, 83–128, 2015

Millennial erosion rates across the Pamir dominated by topographic factors

M. C. Fuchs et al.

of India–Eurasia convergence in the Pamir-Hindu Kush from GPS measurements, Geophys. Res. Lett., 37, L041737, doi:10.1029/2009GL041737, 2010. 86, 89
Molnar, P. and England, P.: Late Cenozoic uplift of mountain ranges and global climate change: chicken or egg?, Nature, 346, 29–34, 1990. 86
Montgomery, D. R. and Brandon, M. T.: Topographic controls on erosion rates in tectonically active mountain ranges, Earth Planet. Sc. Lett., 201, 481–489, 2002. 86, 87, 96
Nishiizumi, K., Imamura, M., Caffee, M. W., Southon, J. R., Finkel, R. C., and McAninch, J.: Absolute calibration of ^{10}Be AMS standards, Nucl. Instrum. Meth. B, 258, 403–413, 2007. 94
Norton, K. P. and Vanacker, V.: Effects of terrain smoothing on topographic shielding correction factors for cosmogenic nuclide-derived estimates of basin-averaged denudation rates, Earth Surf. Proc. Land., 34, 145–154, 2009. 95, 96
Norton, K. P., Abbuhl, L. M., and Schlunegger, F.: Glacial conditioning as an erosional driving force in the Central Alps, Geology, 38, 655–658, 2010. 90, 96
Ouimet, W. B., Whipple, K. X., and Granger, D. E.: Beyond threshold hillslopes: channel adjustment to base-level fall in tectonically active mountain ranges, Geology, 37, 579–582, 2009. 87
Pohl, E., Knoche, M., Gloaguen, R., Andermann, C., and Krause, P.: The hydrological cycle in the high Pamir Mountains: how temperature and seasonal precipitation distribution influence stream flow in the Gunt catchment, Tajikistan, Earth Surf. Dynam. Discuss., 2, 1155–1215, doi:10.5194/esurfd-2-1155-2014, 2014. 109, 110
QGIS Development Team: QGIS Geographic Information System, Open Source Geospatial Foundation, available at: http://qgis.osgeo.org (last access: 6 August 2014), 2010. 95
R Core Team: R: a Language and Environment for Statistical Computing, R Foundation for Statistical Computing, Vienna, Austria, available at: http://www.R-project.org (last acess: 10 November 2014), 2013. 96
Reigber, C., Michel, G. W., Galas, R., Angermann, D., Klotz, J., Chen, J. Y., Papschev, A., Arslanov, R., Tzurkov, V. E., and Ishanov, M. C.: New space geodetic constraints on the distribution of deformation in Central Asia, Earth Planet. Sc. Lett., 191, 157–165, 2001. 86
Robinson, A. C.: Geologic offsets across the northern Karakorum fault: Implications for its role and terrane correlations in the western Himalayan-Tibetan orogen, Earth Planet. Sc. Lett., 279, 123–130, 2009. 89

ESURFD
3, 83–128, 2015

Röhringer, I., Zech, R., Abramowski, U., Sosin, P., Aldahan, A., Kubik, P. W., Zöller, L., and Zech, W.: The late Pleistocene glaciation in the Bogchigir Valleys (Pamir, Tajikistan) based on ^{10}Be surface exposure dating, Quaternary Res., 78, 590–597, 2012. 90, 103

Schaller, M., von Blanckenburg, F., Hovius, N., and Kubik, P. W.: Large-scale erosion rates from in situ-produced cosmogenic nuclides in European river sediments, Earth Planet. Sc. Lett., 188, 441–458, 2001. 87, 96, 104

Scherler, D., Bookhagen, B., and Strecker, M. R.: Tectonic control on ^{10}Be-derived erosion rates in the Garhwal Himalaya, India, J. Geophys. Res.-Earth, 119, 83–105, 2014. 107, 108, 110

Schmidt, J., Hacker, B. R., Ratschbacher, L., Konstanze, S. B., Stearns, M., Kylander-Clark, A., Cottle, J. M., Alexander, A., Webb, G., Gehrels, G., and Minaev, V.: Cenozoic deep crust in the Pamir, Earth Planet. Sc. Lett., 312, 411–421, 2011. 89

Schneider, F. M., Yuan, X., Schurr, B., Mechie, J., Sippl, C., Haberland, C., Minaev, V., Oimahmadov, I., Gadoev, M., Radjabov, N., Abdybachaev, U., Orunbaev, S., and Negmatullaev, S.: Seismic imaging of subducting continental lower crust beneath the Pamir, Earth Planet. Sc. Lett., 375, 101–112, 2013. 89

Schwab, M., Ratschbacher, L., Siebel, W., McWilliams, M., Minaev, V., Lutkov, V., Chen, F., Stanek, K., Nelson, B., Frisch, W., and Wooden, J. L.: Assembly of the Pamirs: age and origin of magmatic belts from the southern Tien Shan to the southern Pamirs and their relation to Tibet, Tectonics, 23, TC4002, doi:10.1029/2003TC001583, 2004. 89, 122

Siame, L., Bellier, O., Braucher, R., Sébrier, M., Cushing, M., Bourlès, D., Hamelin, B., Baroux, E., de Voogd, B., Raisbeck, G., and Yiou, F.: Local erosion rates versus active tectonics: cosmic ray exposure modelling in Provence (south-east France), Earth Planet. Sc. Lett., 220, 345–364, 2004. 95

Sippl, C., Schurr, B., Yuan, X., Mechie, J., Schneider, F. M., Gadoev, M., Orunbaev, S., Oimahmadov, I., Haberland, C., Abdybachaev, U., Minaev, V., Negmatullaev, S., and Radjabov, N.: Geometry of the Pamir-Hindu Kush intermediate-depth earthquake zone from local seismic data, J. Geophys. Res.-Sol. Ea., 118, 1438–1457, 2013. 89, 90

Stone, J. O.: Air pressure and cosmogenic isotope production, J. Geophys. Res.-Sol. Ea., 105, 23753–23759, 2000. 94, 95, 120

Strahler, A., Muchoney, D., Borak, J., Friedl, M., Gopal, S., Lambin, E., and Moody, A.: MODIS Land Cover Product Algorithm Theoretical Basis Document (ATBD) Version 5.0, Center for Remote Sensing, Department of Geography, Boston University, Boston, MA, 1–59, 1999. 90, 95, 119, 122

ESURFD

3, 83–128, 2015

Millennial erosion rates across the Pamir dominated by topographic factors

M. C. Fuchs et al.

Strecker, M. R., Frisch, W., Hamburger, M. W., Ratschbacher, L., Semiletkin, S., Zamoruyev, A., and Sturchio, N.: Quaternary deformation in the Eastern Pamirs, Tadzhikistan and Kyrgyzstan, Tectonics, 14, 1061–1079, 1995. 89, 90

Stübner, K., Ratschbacher, L., Weise, C., Chow, J., Hofmann, J., Khan, J., Rutte, D., Sperner, B., Pfänder, J. A., Hacker, B. R., Dunkl, I., Tichomirowa, M., Stearns, M. A., Bahram, I., Gadoev, M., Gloaguen, R., Jonckheere, R., Kanaev, E., Minaev, V., Oimahmadoc, I., Rajabov, N., and Stanek, K. P.: The giant Shakhdara migmatitic gneiss dome, Pamir, India–Asia collision zone, 2. Timing of dome formation, Tectonics, 32, 1404–1431, 2013. 86, 89, 105, 122

Trifonov, V. G.: Late Quaternary tectonic movements of western and central Asia, Geol. Soc. Am. Bull., 89, 1059, doi:10.1130/0016-7606(1978)89<1059:LQTMOW>2.0.CO;2, 1978. 89

von Blanckenburg, F.: The control mechanisms of erosion and weathering at basin scale from cosmogenic nuclides in river sediment, Earth Planet. Sc. Lett., 237, 462–479, 2005. 87, 88, 91, 92, 95, 96, 104, 105

Wolman, J. G. and Miller, J. P.: Magnitude and frequency of forces in geomorphic processes, J. Geol., 68, 54–74, 1960. 104

Zech, R., Abramowski, U., Glaser, B., Sosin, P., Kubik, P. W., and Zech, W.: Late Quaternary glacial and climate history of the Pamir Mountains derived from cosmogenic ^{10}Be exposure ages, Quaternary Res., 64, 212–220, 2005. 90, 95, 103

Table 1. Details on sampling sites and related upstream drainage area (sample basin). Ice: permanent ice and snow cover based on the year 2010 from MODIS MCD12Q1 (Strahler et al., 1999), the given uncertainty represents the standard deviation of MODIS MCD12Q1 between 1998 and 2012. Altitude, slope and precipitation represent the median of the value distribution within sampled basins (see Fig. 2) calculated from the ASTER GDEM (30 m resolution). The rainfall data reflects the annual mean precipitation based on the Tropical Rainfall Measuring Mission (TRMM) product 3B42 V7, 1998–2012 (Huffman et al., 1997, 2007). Bold letters in sample names indicate notations used in the text and figures.

Sample	River	Location			Sample basin				
		Lon [° E]	Lat [° N]	Altitude [m a.s.l.]	Area [km^2]	Ice [%]	Altitude [m a.s.l.]	Slope [°]	TRMM [mm yr^{-1}]
Panj:									
TA0909**23A**	Panj	70.177	37.901	731	71 727	16.3 ± 2.9	4213	24.3	316
TA0909**08B**	Panj	70.787	38.456	1220	67 749	17.1 ± 3.0	4255	24.1	309
Vanj:									
TA0909**02A**	Vanj	71.378	38.293	1551	2079	37.0 ± 6.5	3869	31.4	364
Bartang:									
TA0909**01C**	Bartang	71.610	37.490	2030	29 243	13.6 ± 2.4	4351	21.4	239
TA1108**08N**	Aksu	73.965	38.161	3603	13 548	4.0 ± 0.7	4283	14.5	176
Gunt:									
TA0908**31B**	Gunt	71.527	37.490	2078	8437	18.7 ± 3.3	4294	23.3	376
TA1108**30P**	Shakhdara	71.845	37.210	2785	3507	13.5 ± 2.4	4281	20.8	390
southern Panj:									
TA0908**28C**	Panj	71.460	37.220	2275	15 230	26.1 ± 4.6	4519	23.8	298
TA0908**25C**	Panj	71.596	36.730	2491	13 625	28.2 ± 4.9	4574	23.2	290
TA1108**24O**	Panj	72.206	36.929	2754	11 064	29.2 ± 5.1	4591	21.6	272
TA1108**23P**	(Pamir)	72.737	37.173	3552	84	55.1 ± 9.6	4770	25.6	321

ESURFD

3, 83–128, 2015

Table 2. Parameters and results of erosion rate calculation. AMS measurements were performed at DREAMS, Helmholtz-Zentrum Dresden-Rossendorf. The ^{10}Be concentrations are corrected for processing blanks ($^{10}Be/^{9}Be$ ratios of 2.0×10^{-15} and 2.1×10^{-15}, i.e. 0.3–1.7 % of the sample values). The effective production rate represents the sum of the neutron- and muon- (fast and stopped muons) induced production of ^{10}Be in quartz (P_{sum}), calculated using the scaling system of Stone (2000), and corrected for topographic shielding using the method of Codilean (2006). The values for individual basins are based on the arithmetic mean. T_{ave} gives the average time needed to erode the typical attenuation depth of ~ 60 cm as a proxy of "cosmogenic memory", describing the time over which the cosmogenic nuclide inventory averages. Bold letters in sample names indicate notations used in the text and figures.

Sample	AMS ^{10}Be conc. [$\times 10^4$ at g^{-1}]	Production rate P_{sum} [at g^{-1} yr^{-1}]	Shielding [factor]	Erosion rate [mm yr^{-1}]	T_{ave} [yr]
Panj:					
TA0909**23A**	5.7 ± 0.2	70.5 ± 17.3	0.92 ± 0.06	0.68 ± 0.23	880
TA0909**08B**	6.7 ± 0.2	72.4 ± 17.3	0.92 ± 0.06	0.59 ± 0.20	1010
Vanj:					
TA0909**02A**	1.9 ± 0.1	52.0 ± 13.3	0.87 ± 0.06	1.45 ± 0.56	410
Bartang:					
TA0909**01C**	5.3 ± 0.2	79.5 ± 12.8	0.93 ± 0.06	0.83 ± 0.22	720
TA1108**08N**	98.5 ± 2.1	80.2 ± 11.0	0.95 ± 0.04	0.05 ± 0.01	13 010
Gunt:					
TA0908**31B**	11.1 ± 0.4	73.1 ± 13.6	0.92 ± 0.06	0.37 ± 0.11	1640
TA1108**30P**	25.5 ± 1.5	75.4 ± 12.0	0.93 ± 0.06	0.16 ± 0.05	3650
southern Panj:					
TA0908**28C**	5.9 ± 0.3	78.3 ± 16.5	0.92 ± 0.06	0.74 ± 0.24	810
TA0908**25C**	7.6 ± 0.3	80.4 ± 16.4	0.92 ± 0.06	0.58 ± 0.18	1030
TA1108**24O**	6.3 ± 0.6	81.7 ± 14.2	0.93 ± 0.06	0.72 ± 0.24	830
TA1108**23P**	5.7 ± 0.2	84.7 ± 11.1	0.89 ± 0.06	0.79 ± 0.19	760

ESURFD
3, 83–128, 2015
Millennial erosion rates across the Pamir dominated by topographic factors
M. C. Fuchs et al.

Title Page
Abstract Introduction
Conclusions References
Tables Figures
◄ ►
Back Close
Full Screen / Esc
Printer-friendly Version
Interactive Discussion

ESURFD
3, 83–128, 2015

Millennial erosion rates across the Pamir dominated by topographic factors

M. C. Fuchs et al.

Table 3. Approximated erosion rates of sub-basins using weighting factors that account for basin area (*a*) and basin slope (*s*). The weighting factors *a* and *s* are applied to determine variations in erosion within large basins when the rates are know (determined based on measured ^{10}Be concentrations and respective productions rates) for the entire basin and one of its sub-basins (ε: erosion rate, total: sample data for entire basin, up: sample data for upper sub-basin, down: inferred rate for lower sub-basin using the *area* or *slope*-based weighting factors, *a*: area factor describing the proportion of the respective sub-basin normalized to 1, *s*: slope factor describing the slope variations of sub-basins normalized to 1).

Basin	Erosion rate [mm yr^{-1}]				Basin area		Basin slope	
	ε_{total}	ε_{up}	$\varepsilon_{down(area)}$	$\varepsilon_{down(slope)}$	a_{up}	a_{down}	s_{up}	s_{down}
Gunt	0.37 ± 0.11	0.16 ± 0.05	0.53 ± 0.16	0.54 ± 0.16	0.44	0.56	0.45	0.55
Bartang	0.83 ± 0.22	0.05 ± 0.01	1.64 ± 0.38	1.23 ± 0.29	0.51	0.49	0.34	0.66
Southern Panj (TA25C)	0.58 ± 0.18	0.72 ± 0.24	0.02 ± 0.01	0.46 ± 0.15	0.80	0.20	0.47	0.53
Southern Panj (TA28C)	0.74 ± 0.24	0.58 ± 0.18	1.81 ± 0.57	0.89 ± 0.28	0.87	0.13	0.49	0.51

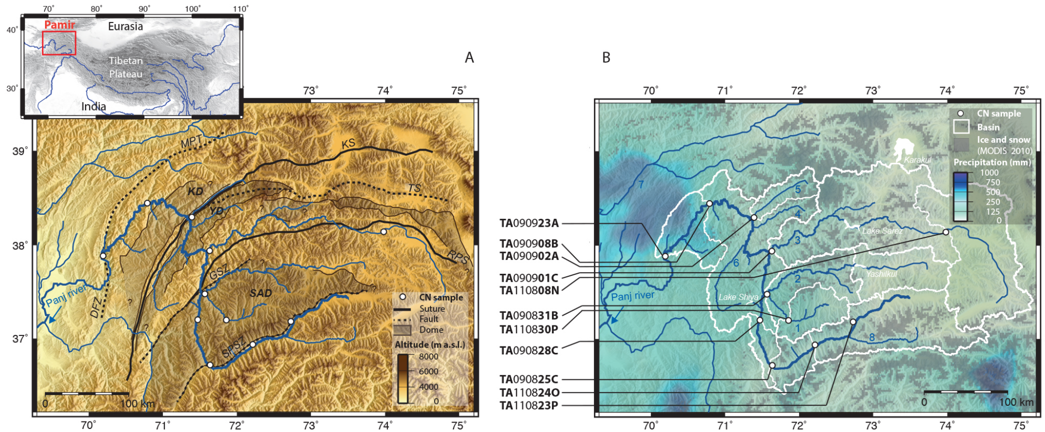

Figure 1. Regional setting of the Panj river system and sample locations (CN: cosmogenic nuclide, a.s.l.: above sea level). **(a)** Topography and main tectonic structures (DFZ: Darvaz Fault Zone, MPT: Main Pamir Thrust, KS: Kunlun Suture, TS: Tanymas Suture, RPS: Rushan-Psart Suture, GSZ: Gunt Shear Zone, SPSZ: Southern Pamir Shear Zone, KD: Kurgovat Dome, YD: Yazgulom Dome, SAD: Shakhdara and Alichur Dome, modified after e.g. Schwab et al., 2004; Stübner et al., 2013). **(b)** Sample locations along the Panj and major tributaries (1: Shakhdara, 2: Gunt, 3: Bartang, 4: Yazgulom, 5: Vanj, 6: Shiva, 7: Vakhsh, 8: Wakhan) and related drainage basins. The climate is shown by the distribution of annual precipitation (TRMM 3B42 V7, 1998–2012, Huffman et al., 1997, 2007) and permanent snow and ice cover (MODIS MCD12Q1, Strahler et al., 1999, year 2010).

ESURFD
3, 83–128, 2015

Millennial erosion rates across the Pamir dominated by topographic factors

M. C. Fuchs et al.

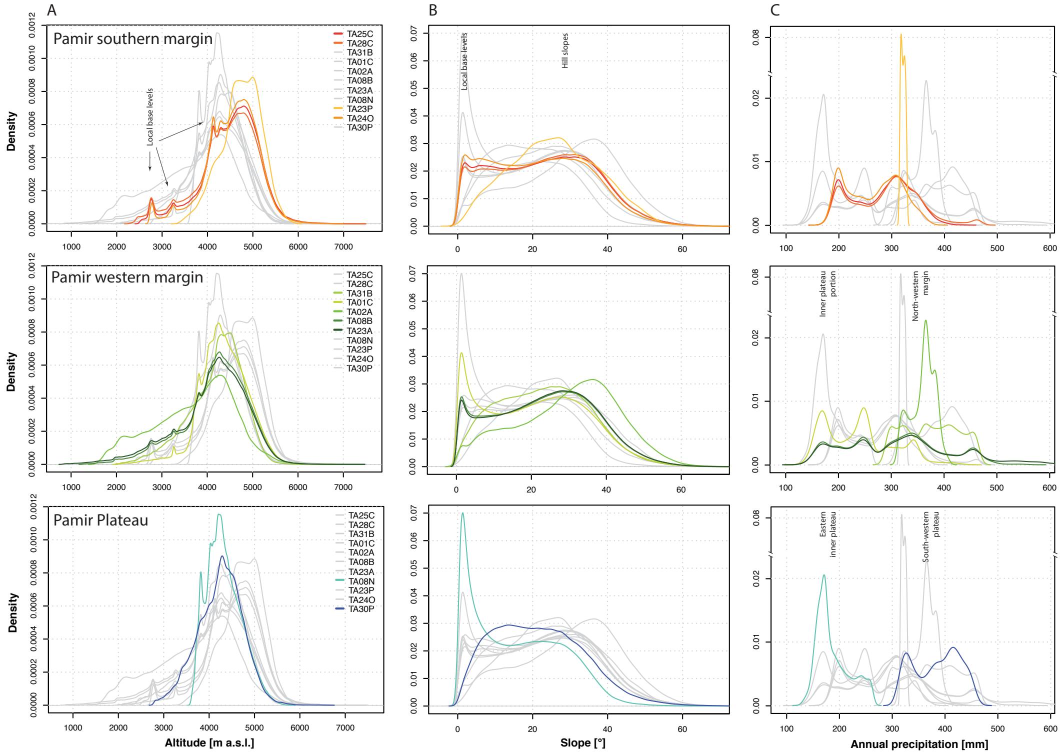

Figure 2. Frequency distributions of altitude **(a)**, slope **(b)** and precipitation **(c)** for individual sample basins grouped due to their location at the southern or western margin of Pamir or at the Pamir Plateau. Relative frequencies of altitude and slope were calculated from a ASTER GDEM of 30 m resolution and precipitation from the TRMM product 3B42 V7 (Huffman et al., 1997, 2007) (notation of basins refers to bold fonts used for sample names in Fig. 1 and Table 1).

ESURFD
3, 83–128, 2015

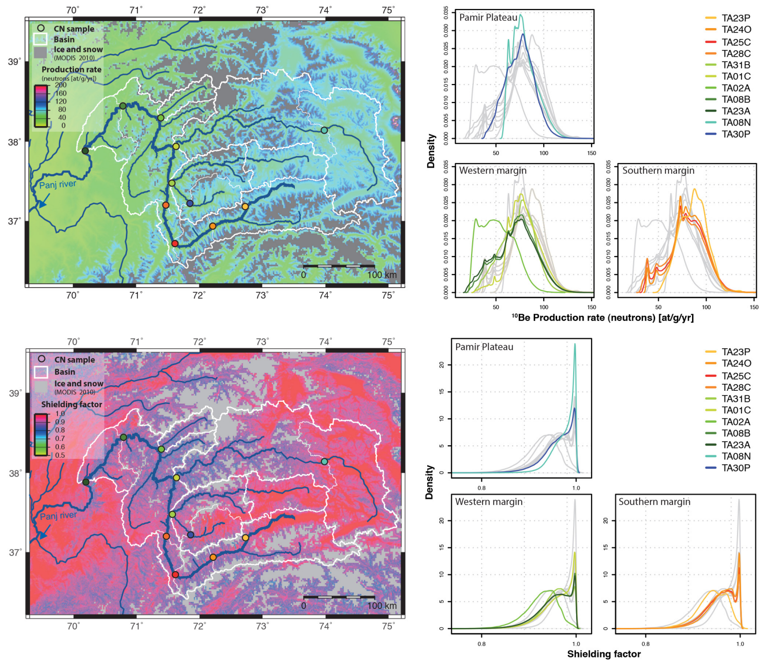

Figure 3. Spatial variations of ^{10}Be production rates and topographic shielding according to the hypsometry of the Pamir, and individual frequency distributions of production and shielding within sampled basins (cf. Figs. 1 and 2). As an example of the spatially variable production, rates are given for the neutron induced ^{10}Be built-up (CN: cosmogenic nuclide, color code for CN sample locations in map refers to individual basins in the legend of frequency distribution plots: reddish: southern Pamir margin, greenish: western Pamir margin, blueish: plateau-related basins, cf. Fig. 1; notation of basins refers to bold fonts used for sample names in Fig. 1 and Table 1).

ESURFD
3, 83–128, 2015

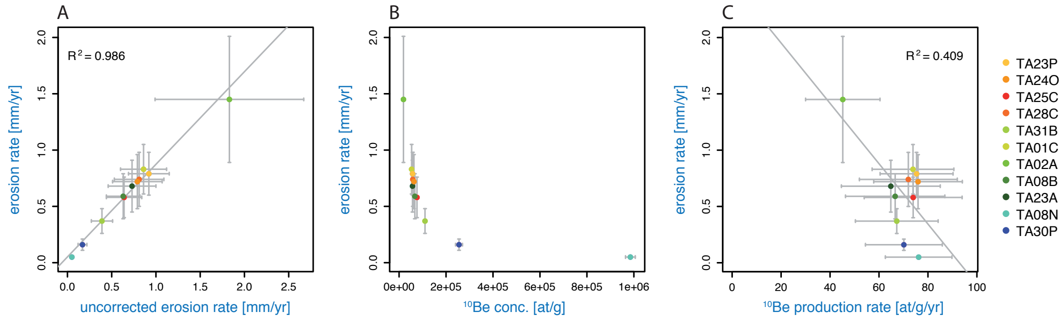

Figure 4. Relationship between basin-wide erosion rates and respective parameters used for calculations and corrections. **(a)** Erosion rates with and without correction for areas covered by permanent snow and ice. **(b)** Exponential relation between erosion and ^{10}Be concentrations from AMS measurements. **(c)** Low variability of production rates corrected for topographic shielding (color code refers to individual basins in the legend, reddish: southern Pamir margin, greenish: western Pamir margin, blueish: plateau-related basins, cf. Fig. 1; notation of basins refers to bold fonts used for sample names in Fig. 1 and Table 1.

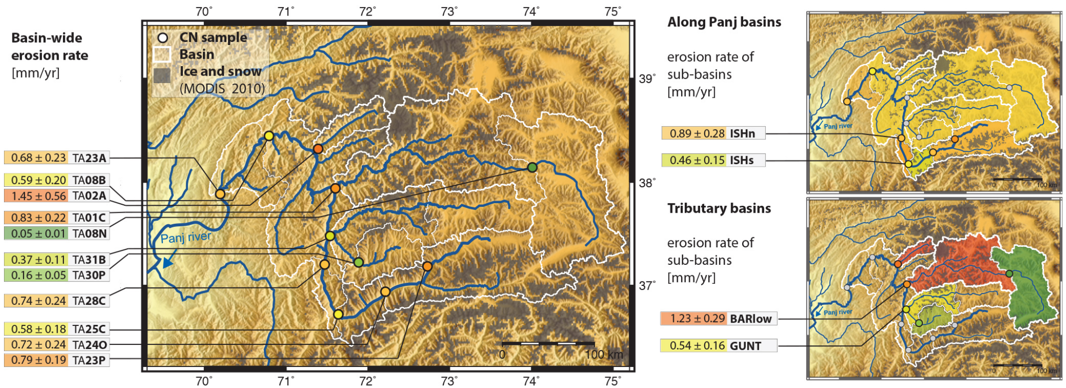

Figure 5. Basin-wide erosion rates of along Panj and major tributary samples (CN: cosmogenic nuclide, color code represents magnitude of erosion with green for low and red for high rates). Calculations base upon AMS measurements of ^{10}Be concentrations in modern fluvial sediments and GDEM processing for production rates and topographic shielding. Erosion rates of the sub-basins ISHn, ISHs, BARlow and GUNT represent slope weighted estimates inferred from sampled basins (respective up and down-stream basins) and using derived measurement results in Eq. (3) (for details see text and Table 3).

ESURFD
3, 83–128, 2015

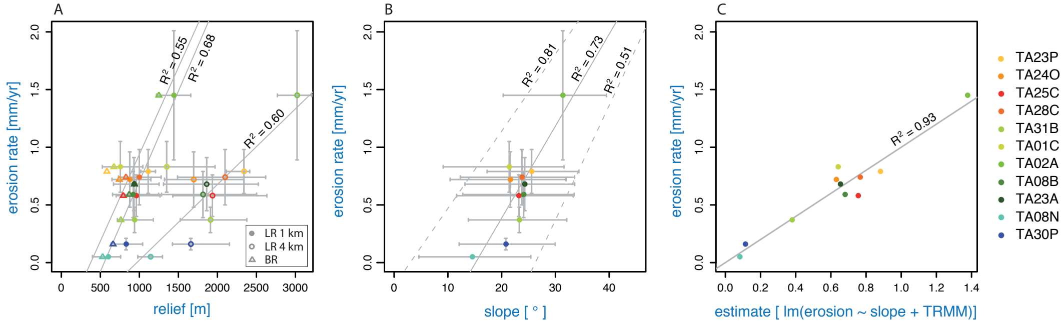

Figure 6. Linear regression analyses for erosion rates and the basin parameters relief **(a)**, slope **(b)** and slope combined with precipitation **(c)**. **(a)** Scale-dependent relief calculation (BR: Basin relief representing the difference between the 0.75 and 0.25 quartiles of basin altitudes, LR: Local relief determining the altitude difference within a moving window of 1 and 4 km, respectively. Values of each basin represent the median and the range between the 0.75 and 0.25 quartiles). **(b)** Basin slopes representing the median of slopes within individual basins. Slope variations are shown according to the 0.25 and 0.75 quartiles. **(c)** Multiple linear regression revealed highest correlation of erosion rates with the 0.75 quartiles of basin slope and TRMM-based precipitation (lm: linear model used for multiple linear regression analyses). Solid lines show the linear regression for median values, dashed lines that of respective quartiles. R^2 gives the correlation coefficient.

ESURFD
3, 83–128, 2015

Millennial erosion rates across the Pamir dominated by topographic factors

M. C. Fuchs et al.

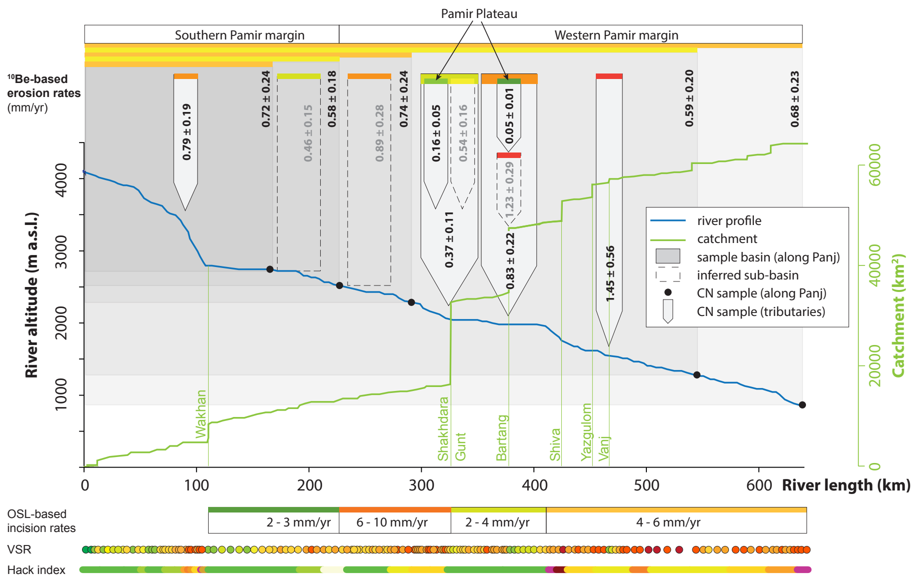

Figure 7. Variation of millennial, basin-averaged erosion rates and fluvial incision along the Panj (CN: cosmogenic nuclide, OSL: optically stimulated luminescence). The along Panj samples (filled circles) represent ^{10}Be-based erosion rates that integrate over related upstream areas (grey shaded areas). Major tributaries and their sub-basins show local differences in erosion between marginal and plateau-related basin portions. The color code illustrates the magnitude of erosion rates (green: low, red: high) and indicates the respective basin area. OSL-based incision rates, valley shape ratios (VSR) and Hack indices (Fuchs et al., 2013, 2014) along the Panj represent the pattern of fluvial incision that determines the lowering of local base levels at the Pamir margins.

ESURFD
3, 83–128, 2015